

1 Word count: ~7500

2 **Revision 2**

3
4 **Tetrahedral aluminum in tourmaline from a spinel-pargasite-metamorphosed mafic-**
5 **ultramafic rock**

6
7 Oleg S. Vereshchagin^{1*}, Yuliya D. Gritsenko^{2,3}, Marina F. Viganina³, Sergey K. Dedushenko⁴, Liudmila A.
8 Gorelova¹, Leonid A. Pautov^{2,5}, Atali A. Agahanov², Irina A. Chernyshova¹, Anatoly A. Zolotarev¹

9
10 1 Saint Petersburg State University, University Embankment 7/9, 199034 St. Petersburg, Russia

11 2 Fersman Mineralogical Museum of the Russian Academy of Sciences, Leninsky Pr. 18-2, Moscow, Russia

12 3 Faculty of Geology, Moscow State University, Vorobievsky Gory, 119991 Moscow, Russia

13 4 National University of Science and Technology MISIS, Leninsky Prospekt 4, 119049 Moscow, Russia

14 5 South Urals Federal Research Center of Mineralogy and Geocology of the Urals Branch of the Russian
15 Academy of Sciences, Ilmensky Reserve 1, 456317 Miass, Russia

16

17 * Corresponding author: o.vereshchagin@spbu.ru

18 ORCID: 0000-0002-4811-2269

19

ABSTRACT

20
21
22
23
24
25
26
27
28
29
30
31
32
33
34
35
36
37
38
39
40
41
42
43

Tourmaline is a widespread borosilicate mineral, which is well known for its variable chemistry. Although major amounts of octahedral Al in tourmaline is commonplace, the occurrence of significant amounts of tetrahedral Al is relatively rare. This paper focuses on tourmaline from the collection of the A.E. Fersman Mineralogical Museum (Russia) originated from Italy with up to 25% of Si replaced by Al at the tetrahedral site. The tourmaline is characterized by optical and scanning electron microscopy, Raman spectroscopy, infrared spectroscopy, Mössbauer spectroscopy, energy-dispersive and wavelength-dispersive X-ray analysis, laser ablation inductively coupled plasma optical emission spectrometry and single crystal X-ray diffraction. The studied tourmaline occurs as transparent dark blue crystals (with equant external morphology) up to 3 mm in size and forms veinlets cutting a (Mg,Al)-rich metamorphosed mafic-ultramafic rock (Mg>>Fe) composed of spinel, pargasite, clinocllore, phlogopite, and hydroxylapatite. The studied tourmaline meets the criteria defining magnesio-lucchesiite and can be compositionally formed via Tschermak-like ($[6]Me^{2+} + [4]Si^{4+} \leftrightarrow [6]Al^{3+} + [4]Al^{3+}$, where $[6]Me^{2+} = Mg, Fe$) or plagioclase-like ($[9]Ca^{2+} + [4]Al^{3+} \leftrightarrow [9]Na^{+} + [4]Si^{4+}$) substitutions. Zones with a relatively high Si content (Si-rich) have pronounced indications of dissolution, while silicon-depleted zones (Si-poor) overgrow Si-rich zones and eventually creates a visible replacement zone of the crystal. We suggest that Si-poor tourmaline result from the Si-rich tourmaline losing Si during a metasomatic process. The resulting empirical crystal-chemical formula for the Si-poor zone is: $X(Ca_{0.95}Na_{0.03}\square_{0.02})_{\Sigma 1.00} Y(Mg_{1.08}Al_{0.98}Fe^{2+}_{0.50}Fe^{3+}_{0.43})_{\Sigma 3.00} Z(Al_{5.91}Fe^{3+}_{0.09})_{\Sigma 6.00} T[(Si_{4.57}Al_{1.43})_{\Sigma 6.00}O_{18}] (BO_3)_3 V(OH)_3 W[O_{0.95}(OH)_{0.05}]_{\Sigma 1.00}$ ($a = 15.9811(2)$, $c = 7.12520(10)$ Å, $R1 = 1.7$ %) and for the Si-rich zone is: $X(Ca_{0.89}Na_{0.11})_{\Sigma 1.00} Y(Mg_{1.55}Al_{0.80}Fe^{2+}_{0.34}Fe^{3+}_{0.31})_{\Sigma 3.00} Z(Al_{5.51}Mg_{0.44}Fe^{3+}_{0.05})_{\Sigma 6.00} T[(Si_{5.35}Al_{0.65})_{\Sigma 6.00}O_{18}] (BO_3)_3 V(OH)_3 W[O_{0.93}(OH)_{0.07}]_{\Sigma 1.00}$ ($a=15.9621(3)$, $c=7.14110(10)$ Å, $R1=1.7$ %). According to *PT* calculations of mineral assemblage stability and comparable data on synthetic $[4]Al$ -rich tourmalines,

44 the studied tourmaline was formed at 600–750 °C and 0.10-0.20 GPa. The formation of tetrahedral
45 Al-rich tourmalines requires several unusual factors: (1) desilication of primary rocks and (2) high
46 temperatures and relatively low pressures.

47 **Keywords:** tourmaline, Tschermak substitution, tetrahedral aluminum, single-crystal X-ray
48 diffraction, Raman spectroscopy, infrared spectroscopy, Mössbauer spectroscopy, LA ICP OES,
49 EMPA.

50

51

INTRODUCTION

52 Tourmaline is a widespread borosilicate mineral (*e.g.*, Henry and Dutrow, 1996; Van Hinsberg
53 et al. 2011; Grew et al., 2017), which could be considered as the main boron host in siliceous crustal
54 rocks (*e.g.*, Dutrow and Henry 2011); its electrical (*e.g.*, Chernyshova et al. 2021) and optical
55 properties (Xia and Kang 2022) make it attractive for use in material sciences. The generalized
56 chemical formula of tourmaline supergroup minerals is $^{[9]}X^{[6]}Y_3^{[6]}Z_6(^{[4]}T_6O_{18})(^{[3]}BO_3)_3V_3W$, where
57 $^{[9]}X = \text{Na, K, Ca, vacancy } (\square), ^{[6]}Y = \text{Li, Mg, Mn}^{2+}, \text{Fe}^{2+}, \text{Al, V}^{3+}, \text{Cr}^{3+}, \text{Fe}^{3+}, \text{Ti}, ^{[6]}Z = \text{Mg, Fe}^{2+}, \text{Al,}$
58 $\text{V}^{3+}, \text{Cr}^{3+}, \text{Fe}^{3+}, ^{[4]}T = \text{Si, Al, B, V} = \text{O, OH, W} = \text{O, OH, F}$ (Henry et al. 2011). These minerals are
59 renowned for their complex crystal chemistry (*e.g.*, Bosi 2011; Vereshchagin et al. 2018; Bačík and
60 Fridrichová 2021). To date, 40 mineral species are recognized within the supergroup, which include
61 more than 15 species-defining elements (The official International Mineralogical Association (IMA)
62 Commission On New Minerals, Nomenclature And Classification (CNMNC) List of Mineral
63 Names).

64 The most obvious feature of tourmaline structure is the six-membered ring of $[TO_4]$
65 tetrahedra, predominantly filled with silicon (*e.g.*, Bosi, 2011; Bačík and Fridrichová, 2021). Long-
66 standing studies of natural (*e.g.*, Ertl et al. 1997; Lussier et al. 2009; Bačík et al. 2013) and synthetic
67 tourmalines (*e.g.*, Rosenberg and Foit 1979; Ertl et al. 2015; Kutzschbach et al. 2016) showed that
68 tetrahedral sites can be occupied by B and Al in addition to Si cations. The substitution of B for Si is
69 mainly related to high pressures and temperatures (*PT*; *e.g.*, Kutzschbach et al. 2016; Ertl et al.
70 2018), while the substitution of Al for Si most likely reflects not only the changes in *PT* conditions
71 (*e.g.*, Rosenberg and Foit 1979), but also the features of the mineral assemblage and mineral
72 chemistry of the host rock (*e.g.*, Bačík et al. 2013).

73 It is important to note that despite the fact that aluminum is a ubiquitous constituent of
74 tourmalines (*e.g.*, Henry et al. 2011), it predominantly fills octahedral sites in the crystal structure

75 while its presence in tetrahedral sites is usually minor to insignificant ($^{[4]}Al < 0.3$ atoms per formula
76 unit (apfu); Lussier et al. 2009). This paper focuses on (1) tourmaline from the collection of the A.E.
77 Fersman Mineralogical Museum (Russia), which contains up to 25% of Si replaced by Al at the
78 tetrahedral site; and (2) its relation to the formation conditions applicable to $^{[4]}Si$ -poor, $^{[4]}Al$ -rich
79 tourmalines.

80 MATERIALS AND METHODS

81 The sample for this study was brought to the collection of the A.E. Fersman Mineralogical
82 Museum (Moscow, Russia) in 1921 (record No. 10997). It was labeled as ‘melanite’ (Ti-bearing
83 andradite) originating from Valtigels bei Sterzing, Tyrol, Austria-Hungary (Figure 1a), which today
84 is known as Faltigl, Alto Adige, Italy. The sample was re-examined during the revision of museum
85 specimens in 2020 and it turned out to be a tourmaline supergroup member.

86 The sample is a 5×6 cm fragment of dark gray fine-grained rock containing a 4×5 cm
87 veinlet with tourmaline crystals (Figure 1b). The crystals were studied using optical and scanning
88 electron microscopy (SEM), Fourier-Transform infrared spectroscopy (FTIR), Mössbauer
89 spectroscopy (MS), Raman spectroscopy, energy-dispersive X-ray (EDS) spectroscopy and
90 wavelength-dispersive X-ray spectroscopy (WDS), laser ablation inductively coupled plasma optical
91 emission spectrometry (LA-ICP-OES) and single crystal X-ray diffraction (SCXRD).

92 The chemical composition of the crystals was analyzed on an epoxy-mounted, polished, and
93 carbon-coated sample with the Superprobe 733 (JEOL, Japan) electron microprobe (WDS mode; 20
94 kV, beam current of 25 nA, 10 μ m beam diameter at the sample surface) and a S-3400 N (Hitachi,
95 Japan) scanning electron microscope equipped with an AzTec Energy XMax 20 (Oxford, UK)
96 spectrometer (EDS mode; 20 kV, beam current of 1 nA, 1 μ m beam diameter at the sample surface).
97 A series of natural and synthetic standards were employed. The content of B, Be and Li in the
98 tourmaline was determined using LA-ICP-OES with a VARIAN 725 spectrometer (Agilent, USA).

99 The empirical formula of tourmaline was calculated on the basis of 15 ($T + Y + Z$) atoms per
100 formula unit (apfu) considering that: (1) vacancies may occur at the X -site, (2) there was no excess
101 of boron ($B = 3$ apfu, see below). H_2O was calculated based on the electroneutral formula: ${}^V\text{OH}=3$
102 and ${}^W\text{O}/\text{OH}$ ratio, based on $Y + Z + T = 15$ and MS data. Fragments of a zoned tourmaline crystal
103 with low and high Si content (No 1 and 2; Figure 1c; Table 1) were used for Raman spectroscopy
104 and subsequent SCXRD analysis (1-AD23 and 2-AD23, respectively).

105 SCXRD analysis was performed using a XtaLAB Synergy-S (Rigaku Oxford Diffraction,
106 Japan) diffractometer equipped with a HyPix-6000HE detector operated with monochromated
107 MoK α radiation at 50 kV and 40 mA. More than a hemisphere of three-dimensional data was
108 collected (Table 2; Crystallographic Information Files). The data were integrated and corrected for
109 background, Lorentz, and polarization effects. The empirical absorption correction based on
110 spherical harmonics implemented in the SCALE3 ABSPACK algorithm was applied in CrysAlisPro
111 program (Agilent 2012). The SHELXL program package (Sheldrick 2015) was used for all
112 structural calculations. The starting coordinates were taken from Vereshchagin et al. (2021). Site
113 populations at the X , B , T , O(3) (=V) and O(1) (=W) sites follow the standard site preference
114 suggested for tourmaline (*e.g.*, Henry et al. 2011). The cation assignment at the X and T sites follows
115 the results of chemical analysis (Table 1) and bond-length considerations (in case of the T site, Ertl
116 et al. 2018). The occupancy of the Y site was obtained considering the presence of Mg and Fe, and
117 the occupancy of the Z site taking into account the presence of Al and Fe. The B and anion sites
118 were modelled with B and O scattering factors, respectively, and with a fixed occupancy of 1, since
119 the refinement with unconstrained occupancies showed no significant deviations from this value.

120 Raman spectra were collected using a LabRam HR 800 (Horiba Jobin-Yvon, Japan)
121 spectrometer equipped with a BX-41 (Olympus, Japan) microscope in backscattering geometry
122 system at ambient conditions using a 532 nm laser. The confocal hole was 100 μm , and a 1800

123 gr/mm grating was used. The Raman spectra of the unoriented sample were recorded in the range of
124 70–4000 cm^{-1} at a resolution of 2 cm^{-1} and an acquisition time of 100 s. The laser power was
125 focused to the point of a size of $\sim 2 \mu\text{m}^2$ by a 100 \times objective. To improve the signal-to-noise ratio,
126 the number of acquisitions was set to 5.

127 FTIR was performed using a FSM-1201 spectrometer (Russia) in the transmittance mode at
128 room temperature in air over the range of wavenumbers from 400 to 4000 cm^{-1} with an accuracy of
129 $\pm 2 \text{ cm}^{-1}$. The sample was prepared as a suspension of 5 mg of mineral powder in vaseline oil and
130 was placed on a plane-parallel KBr plate. The IR spectrum of the same plate without suspension was
131 used as a reference.

132 Room-temperature absorption Mössbauer spectra were recorded on a MS-1101 spectrometer
133 (Russia) in the constant acceleration mode using a standard ^{57}Co source in a metallic rhodium matrix
134 with an activity of about 2 mCi (RITVERC JSC, Russia). Isomer shifts are related to α -iron. The
135 absorber consisted of about 10 mg powdered tourmaline crystals with the addition of sugar powder
136 (used to ensure random crystallite orientation and increase the total volume of the sample). The
137 resultant sample thickness was about $\sim 0.01 \text{ mg } ^{57}\text{Fe}/\text{cm}^2$. The preliminary collection of the
138 spectrum on a larger velocity scale (between -12 and $+12 \text{ mm s}^{-1}$) does not allow us to detect
139 magnetic interactions. Since the impact of magnetic splitting was not detected, the spectrum was re-
140 collected between -5 and $+5 \text{ mm s}^{-1}$ to improve resolution. The spectrum was fitted using the
141 HappySloth software (<http://happysloth.ru/>).

142 RESULTS

143 Mineral assemblage and tourmaline optical properties

144 Tourmaline forms veinlets cutting a (Mg,Al)-rich rock composed of spinel (spinel-hercynite
145 solid solution, Mg:Fe $\sim 2:1$), pargasite (Mg:Fe $\sim 3:1$), clinocllore (Mg:Fe $\sim 8:1$), phlogopite (Mg:Fe

146 ~8:1), and hydroxylapatite. In addition, allanite-(Ce) containing $Ln_2O_3 \sim 12-15$ wt. %, ($Ln = La, Ce,$
147 Nd) and zircon were found as inclusions within the tourmaline in question.

148 Tourmaline occurs as short prismatic to equant crystals up to 3 mm in size (Figure 1a-d). The
149 crystals are transparent, with vitreous luster; brittle, with irregular fracture. The color of tourmaline
150 is dark deep blue, with a white streak. In thin section, it is strongly pleochroic from dark deep blue
151 to grey. It is uniaxial (-), refraction indices measured in Si-poor zone (for more details see below)
152 are: $\omega = 1.666(2)$, $\varepsilon = 1.642(2)$ (589 nm).

153 **Chemical composition**

154 All tourmaline crystals under study are chemically zoned (a typical zone size 20-200 μm ;
155 Fig. 1). The main tetrahedral cation is Si (4.57-5.47 apfu; Table 1). Zones with relatively high Si
156 content (Si-rich) have pronounced textures consistent with dissolution (Figure 1c-d). In contrast, a
157 silicon-depleted zone (Si-poor) overgrows the Si-rich zones and crosscuts the crystal.

158 The tourmaline belongs to the calcic group (Ca 0.83-0.95 apfu; Table 1) and oxy-subgroup
159 (O 0.72-0.95 apfu). The maximum aluminum content in the tetrahedral site reaches 25% and no
160 tetrahedral boron is present (according to LA-ICP-OES, FTIR, Raman spectroscopy and SCXRD
161 (see below)). Aluminum is also the main octahedral cation (6.22-6.91 apfu) and is present in both *Y*-
162 and *Z*-sites as its content is always higher than 6 apfu. All zones being investigated are Mg-rich (Mg
163 1.06-2.08 apfu) and Fe-bearing (Fe_{total} 0.55-1.02 apfu). The content of Li and Be was found to be
164 negligible (<0.1 wt.%). No excess of boron was found by LA-ICP-OES and it was assumed to be
165 stoichiometric (3.00 B apfu) in accordance with the results of FTIR, Raman spectroscopy and
166 SCXRD. This is consistent with the previous studies indicating that $^{[4]}B$ is consistently absent in
167 Mg-rich tourmalines (Lussier et al. 2009).

168 The studied tourmaline meets the criteria defining magnesio-lucchesiite as follows: Ca is
169 dominant at the *X*-site, Mg is dominant at the *Y*-site, Al is dominant at the *Z*-site, O is dominant at

170 the *W*-site. It is worth noting that both octahedral and tetrahedral Al is not species defining in
171 magnesio-lucchesiite and should be ignored (Henry et al. 2011; Scribner et al. 2021). It is interesting
172 to note that the studied tourmaline (magnesio-lucchesiite) contains a significant amounts (up to ~33
173 %) of a hypothetical $\text{CaAl}_3\text{Al}_6(\text{Si}_3\text{Al}_3)\text{O}_{18}(\text{BO}_3)_3(\text{OH})_3\text{O}$ end member, the content of which is almost
174 equal to the content of magnesio-lucchesiite.

175 **Raman spectroscopy**

176 Raman spectra were obtained from the two zones: Si- rich (No. 2, Fig. 1c) and Si- poor (No.
177 1, Fig. 1c). The spectrum obtained from the Si-rich zone (Fig. 2b) has the best resolution compared
178 to the spectrum obtained from the Si-poor sample zone (Fig. 2a). However, the main characteristic
179 Raman bands corresponding to internal vibrations of the structural elements are present in both
180 spectra. It is worth noting that the tourmaline spectrum (Fig. 2b) obtained in the Si-rich zone of the
181 sample (Fig. 1c, point 2) is consistent with that of synthetic oxy-uvite and adachiite (Berryman et al.
182 2016a; Watenphul et al. 2016, respectively).

183 Deformation vibrations of $[\text{TO}_4]$ rings are attributed to the lines at 224, 246, 277, 378 cm^{-1}
184 and symmetrical stretching vibrations of $[\text{TO}_4]$ rings correspond to the line at 490 cm^{-1} (Watenphul
185 et al. 2016). The scattering line at 341 cm^{-1} belongs to the low-frequency bending mode of O-*T*-O in
186 tetrahedral (Watenphul et al. 2016). The scattering line at 564 cm^{-1} corresponds to the highest
187 frequency bending mode of O-*T*-O in tetrahedra $[\text{TO}_4]$ (Watenphul et al. 2016). The lines at 715 and
188 757 cm^{-1} can be attributed to symmetric stretching vibrations of $[\text{BO}_3]^{3-}$ anions (Watenphul et al.
189 2016). Lines at 663 and 987 cm^{-1} are attributed to antisymmetric stretching vibrations of *T*-O bonds
190 in six-membered rings (Watenphul et al. 2016). The scattering line with two components at 1058
191 and 1110 cm^{-1} corresponds to symmetric and antisymmetric stretching vibrations of *T*-O bonds in
192 $[\text{TO}_4]$ groups (Watenphul et al. 2016). A line with low intensity at 1325 cm^{-1} is attributed to
193 antisymmetric stretching vibrations of $[\text{BO}_3]^{3-}$ anions (Watenphul et al. 2016). The absence of lines

194 in the spectral range 3300-3430 cm^{-1} indicates the absence of boron in the tetrahedral position
195 (Kutzschbach et al. 2021). The asymmetric intense band in the range of 3400 - 3590 cm^{-1}
196 corresponds to stretching vibrations of O-H groups at the *V*-site (Peng et al. 1989; Watenphul et al.
197 2016).

198 **Infrared spectroscopy**

199 A relatively small size of compositional zones made it impossible to collect infrared spectra
200 from the Si-rich and Si-poor zones separately. Only the total spectrum was obtained (Figure 3). The
201 FTIR spectrum of the tourmaline in hand (Fig. 3) is consistent with that of adachiite and magnesio-
202 lucchesiite (Nishio-Hamane et al. 2014; Scribner et al. 2021, respectively).

203 The bands corresponding to stretching vibrations of six-membered rings $[(\text{Si,Al})\text{O}_4]_6$,
204 bending vibrations of $[(\text{Si,Al})\text{O}_4]$ and of $[\text{BO}_3]$ groups and lattice modes were observed in the
205 spectral range 400 – 850 cm^{-1} . In this range, the spectra of both samples are practically identical
206 both in shape and in the values of absorption band maxima. In the spectral region 800 – 1200 cm^{-1} ,
207 spectrum (II) exhibits weakly resolved absorption bands. A band with a maximum at 1281 cm^{-1} and
208 a very weak shoulder at 1315 cm^{-1} correspond to stretching vibrations of $[\text{BO}_3]$ -groups, a slightly
209 split band at 982-1026 cm^{-1} can be attributed to stretching vibrations of $[(\text{Si,Al})\text{O}_4]$ -groups.

210 In the spectrum of sample (I), similar absorption bands are clearly resolved into a larger
211 number of components. Thus, the absorption band related to stretching vibrations of $[(\text{Si,Al})\text{O}_4]$ -
212 groups is split into three components 977, 1028 and 1074, cm^{-1} and the absorption band of $[\text{BO}_3]$ -
213 groups has three components with absorption maxima at 1245, 1291 and 1351 cm^{-1} . A two-
214 component band observed in the range 3300–3650 cm^{-1} is attributed to stretching vibrations of OH-
215 groups. A high-frequency component with weak intensity near 3628 cm^{-1} should be attributed to
216 hydroxyl groups at the *W*-site (Nishio-Hamane et al. 2014).

217 **Mössbauer spectroscopy**

218 The relatively small size of the zones did not allow to collect spectra from the Si-rich and Si-
219 poor zones separately. Only the total spectrum was obtained (Figure 4). The Mössbauer spectrum of
220 the tourmaline under study consists of broadened lines of different intensity and can be described by
221 the superposition of two symmetrical doublets (Fe^{3+} : ${}^{\text{RT}}\text{IS}_{\alpha\text{-Fe}}$ 0.41(7), ${}^{\text{RT}}\text{QS}$ 0.88(14) mm s^{-1} ; Fe^{2+} :
222 ${}^{\text{RT}}\text{IS}_{\alpha\text{-Fe}}$ 1.03(8), ${}^{\text{RT}}\text{QS}$ 2.06(15) mm s^{-1}). Along with components (doublets) with isomer shifts
223 typical of $[\text{Fe}^{3+}\text{O}_6]$, it contains components with isomer shifts close to 1.0 mm s^{-1} , which are
224 commonly attributed to $[\text{Fe}^{2+}\text{O}_6]$ (e.g., Bačík et al. 2013; Scribner et al. 2021). At the same time, this
225 isomer shift is completely atypical of divalent iron in octahedral coordination with oxygen (e.g.,
226 Menil 1985). The relative areas of the doublets are similar (~48 and 52 % for Fe^{2+} and Fe^{3+} ,
227 respectively), which indicates that Fe^{2+} : Fe^{3+} ratio is ~1:1. It should be noted that the complication of
228 the spectrum fitting model with the isolation of several different doublets of di- or trivalent iron with
229 close isomer shifts and different quadrupole splitting does not mean that the corresponding iron
230 atoms are at different crystallographic sites. Indeed, the differences in the local environment of iron
231 atoms, which may exist in the sample, may affect the QS value (Dedushenko and Perfiliev 2022).

232 **Crystallography**

233 The tourmalines being under investigation are characterized by minor variations in the unit
234 cell parameters (Table 2). An interesting feature of 1AD-23 is a low ratio of unit cell parameters (c/a
235 0.446), which is one of the lowest among tourmalines (Fig. 5a).

236 X -site scatterings (Crystallographic Information file; Supplementary Table S1-S2) indicate
237 that the $X\text{O}_9$ polyhedron in both cases (samples 1AD-23 and 2AD-23) is almost completely
238 occupied by calcium, which is in a good agreement with the chemical composition (0.95 and 0.89
239 apfu, respectively; Table 1). The $\langle X\text{-O} \rangle$ distances for samples 1AD-23 and 2AD-23 (2.633 and
240 2.632 Å, respectively; Table 3) practically coincide with an analogous distance in the structure of

241 magnesio-lucchesiite (2.626 Å), whose *X* site has a similar composition (Ca_{0.88}Na_{0.12}; Scribner et al.
242 2021; Tables 1, 3).

243 *Y*- and *Z*-site scatterings (Supplementary Table S1-S2) and bond-lengths (Table 3) indicate
244 that the *YO*₆ octahedron in both cases (samples 1AD-23 and 2AD-23) is mainly filled with
245 magnesium and aluminum (Mg>Al), while the *ZO*₆ octahedron is mainly filled with aluminum (see
246 below). All divalent iron was assumed to be present at the *Y*-site only in accordance with the
247 previous studies (e.g., Bačík et al., 2013; Nishio-Hamane et al., 2014), while trivalent iron fills both
248 non-equivalent octahedral sites (mainly *YO*₆). The <*Y*-O> distances for samples 1AD-23 and 2AD-
249 23 (2.025 and 2.021 Å, respectively) are significantly higher than the <*Y*-O> distance in synthetic
250 ^{*Y,Z*}Al-rich tourmaline (<^{*Y*}Al-O>=1.928 Å; Marler et al., 2002). This indicates the presence of large
251 cations (Mg and Fe; Table 1) at the *YO*₆ octahedron as ^[6]Al³⁺ < ^[6]Fe³⁺ < ^[6]Mg²⁺ < ^[6]Fe²⁺ (0.535 <
252 0.645 < 0.72 < 0.78 Å; Shannon, 1976). The <*Z*-O> distances for samples 1AD-23 and 2AD-23
253 (1.916 and 1.920 Å, respectively) are close but slightly higher than the <*Z*-O> distance in synthetic
254 ^{*Y,Z*}Al-rich tourmaline (<^{*Z*}Al-O>=1.914 Å; Marler et al., 2002). This is a sign of the presence of large
255 cations at the *Z*-site.

256 The <*T*-O> distances for samples 1AD-23 and 2AD-23 (1.645 and 1.639 Å, respectively) are
257 significantly higher than the <*T*-O> distance in ^[4]Al-free tourmaline (<^{*T*}Si-O>=1.622 Å; Scribner et
258 al., 2021) and represent the highest known values within the tourmaline supergroup. Interestingly,
259 the <*T*-O> distances for samples 1AD-23 are even higher than in the structure of Ge-rich tourmaline
260 (<*T*-O>=1.640 Å; Setkova et al. 2023), which also indicates unusually low contents of tetrahedral
261 silicon ^[4]Ge ≈ ^[4]Al > ^[4]Si (0.39 > 0.39 > 0.26 Å; Shannon, 1976). The <*T*-O> distances for samples
262 1AD-23 and 2AD-23 (Fig. 5b) are also much higher than those in the crystal structure of adachiite
263 (1.634 Å; Nishio-Hamane et al. 2014) and magnesio-lucchesiite (1.634 Å, Scribner et al. 2021).

264 The occurrence of (OH) groups only at the O(3) site and mixed (O,OH) at O(1) site was
265 proposed based on EDX, MS and examination of bond-valence sums (Supplementary Table S3-4).
266 Bond valence sums on O1 site is ~ 1.5, indicating O>OH. Bond valence sums on O3 site is ~ 1,
267 indicating OH only.

268 The resulting empirical crystal-chemical formula for 1AD-23 is: $X(\text{Ca}_{0.95}\text{Na}_{0.03}\square_{0.02})_{\Sigma=1.00}$
269 $Y(\text{Mg}_{1.08}\text{Al}_{0.98}\text{Fe}^{2+}_{0.50}\text{Fe}^{3+}_{0.43})_{\Sigma=3.00}$ $Z(\text{Al}_{5.91}\text{Fe}^{3+}_{0.09})_{\Sigma=6.00}$ $T[(\text{Si}_{4.57}\text{Al}_{1.43})_{\Sigma=6.00}\text{O}_{18}]$ $(\text{BO}_3)_3$ $V(\text{OH})_3$
270 $W[\text{O}_{0.95}(\text{OH})_{0.05}]_{\Sigma=1.00}$ and for 2AD-23 is: $X(\text{Ca}_{0.89}\text{Na}_{0.11})_{\Sigma=1.00}$ $Y(\text{Mg}_{1.55}\text{Al}_{0.80}\text{Fe}^{2+}_{0.34}\text{Fe}^{3+}_{0.31})_{\Sigma=3.00}$
271 $Z(\text{Al}_{5.51}\text{Mg}_{0.44}\text{Fe}^{3+}_{0.05})_{\Sigma=6.00}$ $T[(\text{Si}_{5.35}\text{Al}_{0.65})_{\Sigma=6.00}\text{O}_{18}]$ $(\text{BO}_3)_3$ $V(\text{OH})_3$ $W[\text{O}_{0.93}(\text{OH})_{0.07}]_{\Sigma=1.00}$.

272 DISCUSSION

273 All zones of the studied tourmaline can be compositionally formed via Tschermak-like
274 substitution ($[^6\text{Me}^{2+}+[^4]\text{Si}^{4+}] \leftrightarrow [^6\text{Al}^{3+}+[^4]\text{Al}^{3+}]$, where $^6\text{Me}^{2+}=\text{Mg, Fe}$; Fig. 6a). The tourmaline in
275 question has a rather high and constant content of calcium (0.83-0.95 apfu; Table 1), however
276 another substitution may be playing an important role in ^4Al -enriched tourmalines: $^9\text{Ca}^{2+} + ^4\text{Al}^{3+}$
277 $\leftrightarrow ^9\text{Na}^+ + ^4\text{Si}^{4+}$ (plagioclase-like or paragonite / margarite-like; Fig. 6b). Both substitutions are
278 possible and further research is required to show which of the mechanisms is more often (more
279 fully) implemented in tourmaline supergroup minerals.

280 It was previously shown that the addition of an Al_2O_3 component to a simple MgO-SiO_2-
281 H_2O system results in a pressure-temperature dependency of Tschermak substitution in antigorite; it
282 was also demonstrated that ^4Al in serpentine can be used to constrain metamorphic conditions
283 (Padrón-Navarta et al. 2013). In general, the operation of this type of substitution to enhance ^4Al
284 will be favored by an increasing temperature and bulk compositions that are aluminous and, to a
285 lesser extent, silica poor (e.g., Pattison 1987; Padrón-Navarta et al. 2013).

286 The studied tourmaline is characterized by the presence of complex zoning, in which the Si-
287 rich zones ($\text{Si} > 5$ apfu) are always highly dissolved (have uneven boundaries; Figure 1c, d).

288 Simultaneously, the silicon-depleted zones (Si ~4.5-5.0 apfu) are the outer zones of the crystal
289 (Figure 1c, d). We can assume the removal of silicon from the early generation of tourmaline (Si-
290 rich zones) and the formation of the second, later generation (Si-poor) with simultaneous
291 recrystallization. It is worth noting both adachiite (Nishio-Hamane et al. 2014) and the studied
292 tourmaline have strong zonation. Possible desilication process is also indirectly confirmed by the
293 absence of quartz (this study; Nishio-Hamane et al. 2014; Scribner et al. 2021). This dissolution and
294 replacement phenomenon of two generations of tourmaline was also described by Henry et al.
295 (2002, 2003).

296 The studied tourmaline was found in spinel-pargasite-clinocllore rocks. Previously, the
297 formation conditions for spinel + pargasite were calculated as 0.2 GPa and 650–750 °C based on
298 pseudosections and simplified phase diagrams of the system (Nozaka et al. 2016). These *PT*
299 parameters seem to be reasonable for the studied tourmaline, since synthetic ^[4]Al-enriched
300 tourmaline in association with spinel and pargasite was obtained under comparable conditions (see
301 below).

302 Both garnet and tourmaline have been mentioned since the beginning of 19th century in
303 various metamorphic rocks from Valtigels bei Sterzing, Italy (e.g., von Senger, 1821; Dobllicka,
304 1852). However, the exact location of the find raises questions, since tourmaline is quite common in
305 this part of Tyrol (e.g., mindat.org) and the area is characterized by relatively high-grade
306 metamorphism (e.g., Zanchetta et al., 2023), which is not fully consistent with the studied rock.
307 Simultaneously, the specimen studied bears a resemblance to the tourmaline from the Elba island,
308 Italy (Dottorini, 2020). To date, it is not possible to accurately answer the question of the origin of
309 the sample from the Fersman Mineralogical Museum with absolute certainty. Therefore, we suggest
310 treating the question of its origin with some caution.

311 Tourmalines with high amounts of $^{[4]}\text{Al}$ (> 0.5 apfu) are rarely found in nature. According to
312 Lussier et al. (2009), there is no clear correspondence between the species of tourmaline and $^{[4]}\text{Al}$
313 content. Ertl et al. (2018) suggested that relatively high amounts of $^{[4]}\text{Al}$ may be expected in Mg-
314 and/or Fe^{2+} -rich tourmalines, especially when they are of aluminous bulk compositions and have
315 experienced high temperature metamorphic conditions.

316 Indeed, all natural $^{[4]}\text{Al}$ -rich tourmalines are Al- and Mg- and/or Fe^{2+} -rich. The studied
317 tourmaline is the most $^{[4]}\text{Al}$ -rich (up to 1.43 apfu; Table 1) species in the tourmaline supergroup
318 known so far. Previously, the highest $^{[4]}\text{Al}$ value (0.95 apfu) was reported in another Ca-, Mg-rich
319 tourmaline (magnesio-lucchesiite; $\text{CaMg}_3\text{Al}_6(\text{Si}_6\text{O}_{18})(\text{BO}_3)_3(\text{OH})_3\text{O}$), which was found in
320 hydrothermal veins embedded in meta-serpentinites within the contact aureole of the Monte
321 Capanne intrusion, Elba Island, Italy (Scribner et al. 2021). Ca, Fe-rich tourmaline (adachiite;
322 $\text{CaFe}_3\text{Al}_6(\text{Si}_5\text{AlO}_{18})(\text{BO}_3)_3(\text{OH})_3(\text{OH})$) ranks third in $^{[4]}\text{Al}$ content (0.84 apfu) and was found in a
323 hydrothermal vein, crosscutting a lateritic metamorphic rock (mainly consisting of corundum and
324 hercynite) near Saiki City, Oita Prefecture, Japan (Nishio-Hamane et al. 2014). Another example
325 worth mentioning is Na, Fe-rich tourmaline (oxy-schorl; $\text{Na}(\text{Fe}^{2+}_2\text{Al})\text{Al}_6(\text{Si}_6\text{O}_{18})(\text{BO}_3)_3(\text{OH})_3\text{O}$)
326 with significant amount of $^{[4]}\text{Al}$ (0.49 apfu), it was found in fracture fillings cutting altered
327 metarhyolite pyroclasts near Zlatá Idka village, Slovak Ore Mountains, Slovak Republic (Bačík et
328 al. 2013). Besides, Na-, Fe-, $^{[4]}\text{Al}$ - enriched tourmaline of the schorl - dravite - ferridravite series
329 with relatively high $^{[4]}\text{Al}$ content (up to 0.42 apfu) were reported from Larderello Geothermal Field,
330 Italy (Cavarretta and Puxeddu, 1990).

331 All synthetic $^{[4]}\text{Al}$ -rich tourmalines are Al-enriched ($\text{Al}_{\text{total}} > 6$ apfu) and contain significant
332 amounts of magnesium or copper. The highest $^{[4]}\text{Al}$ content (up to 1.78 apfu) was reported in Na,
333 Al-rich (0.94, 9.0 apfu, respectively) tourmaline synthesized at 600 °C and 0.1 GPa (Rosenberg et al.
334 1986). However, single-crystal refinement, which could confirm $^{[4]}\text{Al}$ content, has not been done.

335 Besides, synthesis conditions and unit cell parameters (close to synthetic olenite; Marler et al., 2002)
336 indicate that the tetrahedral aluminum content may be overestimated, while the tetrahedral boron
337 content may be underestimated. Lebedev et al. (1998) synthesized a tourmaline containing 0.56 Na,
338 1.74 Mg and 8.34 Al, including 1.08 tetrahedral Al (per formula unit), at 600 °C and 0.15 GPa
339 aluminum (no single-crystal refinement data were provided). Moreover, several of Fe-Mg
340 tourmalines synthesized by Lebedev et al. (1988) are associated with spinel, pargasite and Mg-rich
341 mica group mineral. Consequently, we suggest that the formation conditions for the studied
342 tourmaline could be like those of the syntheses, that is, 600-750 °C and 0.1-0.2 GPa. The next
343 largest ^[4]Al content (up to 0.90 apfu) was found in Cu-rich tourmaline synthesized at 600 °C and
344 0.15 GPa (Lebedev et al. 1988; Vereshchagin et al. 2013; Ertl et al. 2015). ^[4]Al content was proved
345 by single-crystal refinement. Berryman et al. (2015) reported a series of ^[4]Al-rich tourmalines (0.54-
346 0.75 apfu), which were synthesized at a temperature range 500-700 °C and pressure 0.4-3 GPa (no
347 single-crystal refinement data were provided). All of them are Mg-, Al-rich (Mg>2.17, Al>6.55
348 apfu) and most of them (5 out of 6 reported compositions) were obtained at high pressure (3 GPa).
349 These tourmalines belong either to Na-dominant or to X-site vacant species (Berryman et al. 2015).
350 Berryman et al. (2016b) reported another ^[4]Al-rich tourmaline (0.59 apfu), which was synthesized at
351 500 °C and 1 GPa. This tourmaline belongs to the X-site vacant (0.54 apfu) group and is a Mg-, Al-
352 rich (Mg 2.17, Al 6.83 apfu) specie (no single-crystal refinement data were provided). Interestingly,
353 the studies of synthetic tourmalines have shown a weak, but significant correlation of the Tschermak
354 substitution with the pressure of synthesis: ^[4]Al decreases with increasing pressure (Krosse, 1995;
355 Werding, and Schreyer, 1996).

356 It should be noted that most synthetic Al- and Mg- and/or Fe²⁺-rich tourmalines and natural
357 tourmalines contain negligible amounts of tetrahedral aluminum (*e.g.*, Lebedev et al. 1988;
358 Berryman et al. 2015, 2016b). This may be due to (1) the sequence of phase crystallization (earlier

359 phases deplete the solution in silicon), (2) the effect of pressure (as they were obtained at pressure
360 0.15-3 GPa). It is necessary for tourmaline to be undersaturated with silicon so that a significant
361 amount of tetrahedral aluminum appears. Most likely, such conditions can be realized if the silicon
362 content in the system decreases due to the crystallization of the associated phases or desilication (see
363 above).

364 **IMPLICATIONS**

365 According to the modern classification, tourmalines are borosilicates (Henry et al. 2011),
366 since $[TO_4]$ tetrahedra are filled with silicon only in most cases. Previous studies show that in some
367 cases tourmalines can be considered as boro-aluminosilicates, since up to 25% of silicon can be
368 replaced by aluminum in tetrahedra.

369 Our data, together with those previously published on adachiite (Nishio-Hamane et al. 2014),
370 indicate that the high content of aluminum in the tetrahedral site is achieved due to Si removal by
371 the primary generations of tourmaline. Thus, tourmaline enriched in tetrahedral aluminum can be an
372 indicator of metasomatic transformation of rocks. The possibility of the formation of primary
373 tourmaline depleted in silicon seems unlikely, since multiple syntheses of tourmaline in an
374 aluminum-rich medium led to the formation of tourmalines enriched in $^{[4]}B$, but not $^{[4]}Al$ (e.g.,
375 Kutzschbach et al. 2016). However, at present there is too little data to establish this accurately. One
376 can conclude that the formation of such boro-aluminosilicate tourmalines is a rather rare process and
377 is apparently associated with several factors: (1) desilication of primary rocks and (2) high
378 temperatures and relatively low pressures process.

379 We suggest that experiments on the dissolution-recrystallization of tourmalines in silicon-
380 depleted solutions can help answer this question. In addition, in the future such studies will help to
381 more accurately use tourmalines to assess the conditions necessary for its formation.

382 **ACKNOWLEDGMENTS**

383 The authors thank X-ray Diffraction Centre and Geomodel Center of Resource Centre of
384 Saint Petersburg State University for providing instrumental and computational resources. We are
385 thankful to the Associate Editor, Edward Grew, and two reviewers, Aaron Lussier and Darrell
386 Henry, who contributed significantly to improving the quality of the manuscript. This research was
387 funded by Council for Grants of the President of the Russian Federation NSH-1462.2022.1.5 (for
388 OSV, LAG and IAC).

389

390

REFERENCES

391 Agilent (2012) CrysAlis PRO. Agilent Technologies, Oxfordshire, UK.

392 Bačík, P., and Fridrichová, J. (2021) Cation partitioning among crystallographic sites based on
393 bond-length constraints in tourmaline-supergroup minerals. *American Mineralogist*, 106, 851–
394 861.

395 Bačík, P., Cempírek, J., Uher, P., Novák, M., Ozdín, D., Filip, J., Škoda, R., Breiter, K.,
396 Klementová, M., Ďud'a, R., and others (2013) Oxy-schorl, $\text{Na}(\text{Fe}_2\text{Al})\text{Al}_6\text{Si}_6\text{O}_{18}(\text{BO}_3)_3(\text{OH})_3\text{O}$,
397 a new mineral from Zlatá Idka, Slovak Republic and Příbyslavice, Czech Republic. *American*
398 *Mineralogist*, 98, 485–492.

399 Berryman, E.J., Wunder, B., Wirth, R., Rhede, D., Schettler, G., Franz, G., and Heinrich, W. (2015)
400 An experimental study on K and Na incorporation in dravitic tourmaline and insight into the
401 origin of diamondiferous tourmaline from the Kokchetav Massif, Kazakhstan. *Contributions to*
402 *Mineralogy and Petrology*, 169, 1–16.

403 Berryman, E. J., Wunder, B., Ertl, A., Koch-Müller, M., Rhede, D., Scheidl, K., Giester, G., and
404 Heinrich, W. (2016a) Influence of the X-site composition on tourmaline's crystal structure:
405 investigation of synthetic K-dravite, dravite, oxy-uvite, and magnesio-foitite using SREF and
406 Raman spectroscopy. *Physics and Chemistry of Minerals*, 43, 2, 83-102.

407 Berryman, E.J., Wunder, B., Rhede, D., Schettler, G., Franz, G., and Heinrich, W. (2016b) P–T–X
408 controls on Ca and Na distribution between Mg–Al tourmaline and fluid. *Contributions to*
409 *Mineralogy and Petrology*, 171, 1–31.

410 Bosi, F. (2011) Stereochemical constraints in tourmaline: From a short-range to a long-range
411 structure. *Canadian Mineralogist*, 49, 17–27.

412 Cavarretta, G. and Puxeddu, M. (1990) Schorl - dravite - ferridravite tourmalines deposited by
413 hydrothermal magmatic fluids during early evolution of the Larderello Geothermal Field, Italy.
414 *Economic Geology*, Vol. 85, 1236-1251.

415 Chernyshova, I.A., Vereshchagin, O.S., Malyshkina, O. V, Goncharov, A.G., Kasatkin, I.A.,
416 Murashko, M.N., Zolotarev, A.A., and Frank-Kamenetskaya, O. V (2021) Tourmalines
417 pyroelectric effect depending on the chemical composition and cation oxidation state. *Journal*
418 *of Solid State Chemistry*, 303, 122512.

419 Dedushenko, S.K., and Perfiliev, Y.D. (2022) On the correlation of the ^{57}Fe Mössbauer isomer shift
420 and some structural parameters of a substance. *Hyperfine Interactions*, 243, 1–25.

421 Doblícka, K. (1852) *Tirols Mineralien*, 138 pages (in German)

- 422 Dottorini, V. (2020) *Cristallochimica di specie del supergruppo della tormalina dalla Toscana*.
423 Master thesis, University Pisa, 284 pages.
- 424 Dutrow, B., and Henry, D. (2011) Tourmaline: a geologic DVD. *Elements*, 7, 301–306.
- 425 Ertl, A., Pertlik, F., and Bernhardt, H.-J. (1997) Investigations on Olenite with Excess Boron from
426 the Koralpe, Styria, Austria. *Österr. Akad. Wiss., Math.-naturwiss. Kl. Abt. I, Anzeiger*, 3–10.
- 427 Ertl, A., Vereshchagin, O.S., Giester, G., Tillmanns, E., Meyer, H.P., Ludwig, T.,
428 Rozhdestvenskaya, I. V., and Frank-Kamenetskaya, O. V. (2015) Structural and chemical
429 investigation of a zoned synthetic Cu-rich tourmaline. *Canadian Mineralogist*, 53, 209–220.
- 430 Ertl, A., Henry, D.J., and Tillmanns, E. (2018) Tetrahedral substitutions in tourmaline: a review.
431 *European Journal of Mineralogy*, 30, 465–470.
- 432 Grew, E. S., Hystad, G., Hazen, R.M., Krivovichev, S.V. and Gorelova, L. A. (2017) How many
433 boron minerals occur in Earth's upper crust? *American Mineralogist*, 102, 8, 1573–1587.
- 434 Henry, D.J. and Dutrow, B.L. (1996) Metamorphic tourmaline and its petrologic applications. In
435 *Boron: Mineralogy, Petrology and Geochemistry* (E.S. Grew & L.M. Anovitz, eds.).
436 Mineralogical Society of America, *Reviews in Mineralogy* 33, 503–557.
- 437 Henry, D. J., Dutrow, B. L. and Selverstone, J. (2002) Compositional polarity in replacement
438 tourmaline – an example from the Tauern Window, Eastern Alps. *Geological Materials*
439 *Research*, 4, no. 2, 23 p
- 440 Henry, D. J., Dutrow, B. L. and Selverstone, J. (2003) Compositional polarity in replacement
441 tourmaline – an example from the Tauern Window, Eastern Alps. *American Mineralogist*, 88,
442 1399.
- 443 Henry, D.J., Novák, M., Hawthorne, F.C., Ertl, A., Dutrow, B.L., Uher, P., and Pezzotta, F. (2011)
444 Nomenclature of the tourmaline-supergrup minerals. *American Mineralogist*, 96, 895–913.
- 445 Krosse S (1995) Hochdrucksynthese, Stabilität und Eigenschaften der Boeisilikate Dravit und
446 Komerupin sowie Darstellung und Stabilitätsverhalten eines neuen Mg-Al-borates.
447 Unpublished Doctor's thesis Ruhr-Universität, Bochum.
- 448 Kutzschbach, M., Wunder, B., Rhede, D., Koch-Müller, M., Ertl, A., Giester, G., Heinrich, W., and
449 Franz, G. (2016) Tetrahedral boron in natural and synthetic HP / UHP tourmaline: Evidence
450 from Raman spectroscopy, EMPA, and single-crystal XRD. *American Mineralogist*, 101, 93–
451 104.
- 452 Kutzschbach, M., Wunder, B., Wannhoff, I., Wilke, F.D.H., Couffignal, F., and Rocholl, A. (2021)
453 Raman spectroscopic quantification of tetrahedral boron in synthetic aluminum-rich

- 454 tourmaline. *American Mineralogist*, 106, 872–882.
- 455 Lebedev, A.S., Kargalcev, S.V., and Pavlychenko, V.. (1988) Synthesis and properties of tourmaline
456 series Al-Mg-(Na) and Al-Fe-(Na). In *Genetic and Experimental Mineralogy. Growth and*
457 *Properties of Crystals* pp. 58–75. Novosibirsk (in Russian).
- 458 Lussier, A.J., Aguiar, P.M., Michaelis, V.K., Kroeker, S., and Hawthorne, F.C. (2009) The
459 occurrence of tetrahedrally coordinated al and b in tourmaline: An ^{11}B and ^{27}Al MAS NMR
460 study. *American Mineralogist*, 94, 785–792.
- 461 Marler, B., Borowski, M., Wodara, U. and Schreyer, W. (2002) Synthetic tourmaline (olenite) with
462 excess boron replacing silicon in the tetrahedral site: II. Structure analysis. *European Journal of*
463 *Mineralogy*, 14, p. 763 - 771.
- 464 Menil, F. (1985) Systematic trends of the ^{57}Fe Mössbauer isomer shifts in (FeOn) and (FeFn)
465 polyhedra. Evidence of a new correlation between the isomer shift and the inductive effect of
466 the competing bond T-X ($\rightarrow \text{Fe}$) (where X is O or F and T any element with a formal positive
467 charge). *Journal of Physics and Chemistry of Solids*, 46, 763–789.
- 468 Nishio-Hamane, D., Minakawa, T., Yamaura, J., Oyama, T., Ohnishi, M., and Shimobayashi, N.
469 (2014) Adachiite, a Si – poor member of the tourmaline supergroup from the Kiura mine, Oita
470 Prefecture, Japan. *Journal of Mineralogical and Petrological Sciences*, 109, 74–78.
- 471 Nozaka, T., Meyer, R., Wintsch, R.P., and Wathen, B. (2016) Hydrothermal spinel, corundum and
472 diaspore in lower oceanic crustal troctolites from the Hess Deep Rift. *Contributions to*
473 *Mineralogy and Petrology*, 171, 1–14.
- 474 Padrón-Navarta, J.A., Sánchez-Vizcaíno, V.L., Hermann, J., Connolly, J.A.D., Garrido, C.J.,
475 Gómez-Pugnaire, M.T., and Marchesi, C. (2013) Tschermak’s substitution in antigorite and
476 consequences for phase relations and water liberation in high-grade serpentinites. *Lithos*, 178,
477 186–196.
- 478 Pattison, D.R.M. (1987) Variations in Mg/(Mg+Fe), F, and (Fe,Mg)Si = 2Al in pelitic minerals in
479 the Ballachulish thermal aureole, Scotland. *American Mineralogist*, 72, 255–272.
- 480 Peng, M., Ma, H., Chen, L., and Chao, E.C.T. (1989) The polarized Raman spectra of tourmaline.
481 *Annual report of the Director Geophysical Laboratory*, 99–105.
- 482 Rosenberg, P.E., and Foit, F.F. (1979) Synthesis and characterization of alkali-free tourmaline.
483 *American Mineralogist*, 64, 180–186.
- 484 Rosenberg, P.E., Foit, F.F., Jr., and Ekambaram, V. (1986) Synthesis and characterization of
485 tourmaline in the system $\text{Na}_2\text{O}-\text{Al}_2\text{O}_3-\text{SiO}_2-\text{B}_2\text{O}_3-\text{H}_2\text{O}$. *American Mineralogist*, 71, 971-976.

- 486 Shannon, R.D. (1976) Revised effective ionic radii and systematic studies of interatomic distances
487 in halides and chalcogenides. *Acta Crystallographica*, 32, 751–767.
- 488 Scribner, E.D., Cempírek, J., Groat, L.A., Evans, R.J., Biagioni, C., Bosi, F., Dini, A., Hålenius, U.,
489 Orlandi, P., and Pasero, M. (2021) Magnesio-lucchesiite, $\text{CaMg}_3\text{Al}_6(\text{Si}_6\text{O}_{18})(\text{BO}_3)_3(\text{OH})_3\text{O}$, a
490 new species of the tourmaline supergroup. *American Mineralogist*, 106, 862–871.
- 491 Setkova, T. V., Borovikova, E.Y., Zarubina, E.S., Anosova, O.A., Aksenov, S.M., Frolov, K. V.,
492 Balitsky, V.S., Bublikova, T.M., and Pushcharovsky, D.Y. (2023) Crystal Growth and
493 Complex Characterization of Novel Gallium- and Germanium-Rich Tourmalines: Refinement
494 of the Crystal Structure, Cation Distribution, and Raman and Mössbauer Spectroscopy. *Crystal*
495 *Growth and Design*, (in press).
- 496 Sheldrick, G.M. (2015) Crystal structure refinement with SHELXL. *Acta Crystallographica*, C71, 3–
497 8.
- 498 Van Hinsberg, V.J., Henry, D.J., and Marschall, H.R. (2011) Tourmaline: An ideal indicator of its
499 host environment. *Canadian Mineralogist*, 49, 1–16.
- 500 Vereshchagin, O.S., Rozhdestvenskaya, I. V., Frank-Kamenetskaya, O. V., Zolotarev, A.A., and
501 Mashkovtsev, R.I. (2013) Crystal chemistry of Cu-bearing tourmalines. *American*
502 *Mineralogist*, 98, 1610–1616.
- 503 Vereshchagin, O.S., Frank-Kamenetskaya, O. V., Rozhdestvenskaya, I. V., and Zolotarev, A.A.
504 (2018) Incorporation of 3d elements in tourmalines: structural adjustments and stability.
505 *European Journal of Mineralogy*, 30, 917–928.
- 506 Vereshchagin, O.S., Britvin, S.N., Wunder, B., Frank-Kamenetskay, O.V., Wilke, F.D.H., Vlasenko,
507 N.S., Shilovskikh, V.V., Bocharov, V.N., Danilov, D.V. (2021) Ln^{3+} ($\text{Ln}^{3+} = \text{La}, \text{Nd}, \text{Eu}, \text{Yb}$)
508 incorporation in synthetic tourmaline analogues: Towards tourmaline REE pattern explanation.
509 *Chemical Geology*, 584, 120526.
- 510 von Senger, W.E. (1821) *Versuch einer Oryctographie der gefürsteten Grafschaft Tirol*, 110 pages
511 (in German)
- 512 Watenphul, A., Burgdorf, M., Schlüter, J., Horn, I., Malcherek, T., and Mihailova, B. (2016)
513 Exploring the potential of Raman spectroscopy for crystallochemical analyses of complex
514 hydrous silicates: II. Tourmalines. *American Mineralogist*, 101, 970–985.
- 515 Werding, G. and Schreyer, W. (1996), Experimental studies on borosilicates and selected borates.
516 *Mineralogical Society of America, Reviews in Mineralogy*, 33, 117-163.
- 517 Xia, M., and Kang, L. (2022) Tourmaline with ultraviolet optical nonlinearity: Emergent material

- 518 discovery from mineral. *Journal of Alloys and Compounds*, 892, 162235.
- 519 Zanchetta, S., Cucato M., Bove, G., Morelli, C., Poli, S. and Zanchi A. (2023) Note Illustrative della
520 carta Geologica d'Italia in scala 1:50.000, foglio 006 "San Leonardo in Passiria". Servizio
521 Geologico d'Italia - ISPRA, 328 pp.
- 522

Table 1. Chemical composition (wt.%) and atomic proportion in the chemical formula of the studied tourmaline and some related species.

		This work					Nishio-Hamane et al., 2014		Scribner et al., 2021	Bačík et al., 2013		
		1AD-23	2AD-23	1	2	3	4	5	Italy	Canada	Zlatá Idka	
SiO ₂		27.35	31.93	27.43	27.82	29.96	31.06	32.73	34.71	30.26	35.23	33.10
Al ₂ O ₃		42.33	35.22	42.97	40.15	40.67	37.07	34.22	34.36	39.30	26.63	39.81
TiO ₂		bdl	bdl	0.00	0.00	0.00	0.02	0.14	0.00	bdl	1.92	0.02
MgO		4.26	7.97	5.58	5.59	6.74	7.52	8.33	9.16	5.82	7.96	2.31
FeO		3.60	2.37	2.55	3.22	2.14	2.58	2.60	1.34	2.90	4.34	7.97
Fe ₂ O ₃		4.11	2.85	2.61	3.37	2.10	2.67	2.57	1.27	2.86	6.14	bdl
Cr ₂ O ₃		bdl	bdl	bdl	bdl	bdl	bdl	bdl	bdl	bdl	0.10	bdl
V ₂ O ₃		bdl	bdl	bdl	bdl	bdl	bdl	bdl	bdl	bdl	0.08	bdl
Na ₂ O		0.10	0.33	0.31	0.38	0.47	0.46	0.33	1.16	0.37	1.19	1.83
K ₂ O		bdl	bdl	bdl	bdl	bdl	bdl	bdl	bdl	bdl	0.04	bdl
CaO		5.32	4.98	5.10	5.06	4.78	4.68	4.98	3.05	4.93	3.27	0.58
F		bdl	bdl	bdl	bdl	bdl	bdl	bdl	bdl	0.04	0.41	0.26
H ₂ O _{calc}		2.73	2.75	2.96	2.84	2.91	2.91	2.74	2.96	2.60	2.29	2.92
B ₂ O _{3calc}		10.39	10.36	10.48	10.28	10.58	10.44	10.39	10.54	10.41	10.23	10.45
-O=F										0.02	0.17	0.11
Total		100.20	98.76	99.99	98.70	100.35	99.42	99.03	98.55	99.47	99.67	99.18
(Y+Z+T)=15 atoms per formulae unit (apfu)												
<i>X</i>	Ca	0.95	0.89	0.91	0.92	0.84	0.83	0.89	0.62	0.88	0.60	0.10
	Na	0.03	0.11	0.10	0.12	0.15	0.15	0.11	0.28	0.12	0.39	0.59
	K	-	-	-	-	-	-	-	-	-	0.01	0.30
	□	0.02	0.00	0.00	0.00	0.01	0.02	0.00	0.10	0.00	0.00	-
<i>Y</i> + <i>Z</i>	Al	6.91	6.31	6.94	6.71	6.80	6.44	6.22	6.63	6.79	5.31	7.31
	Mg	1.06	1.99	1.38	1.40	1.65	1.87	2.08	0.60	1.45	2.02	0.57
	Fe ²⁺	0.50	0.33	0.35	0.46	0.29	0.36	0.36	1.72	0.40	0.62	1.11
	Fe ³⁺	0.52	0.36	0.33	0.43	0.26	0.33	0.32	-	0.46	0.79	-
	Ti	-	-	0.00	0.00	0.00	0.00	0.02	0.06	-	0.25	-
	Cr	-	-	-	-	-	-	-	-	-	0.01	-
V	-	-	-	-	-	-	-	-	-	0.01	-	
Total		9.00	9.00	9.00	9.00	9.00	9.00	9.00	9.01	9.00	9.01	9.00
<i>T</i>	Si	4.57	5.35	4.55	4.70	4.92	5.17	5.47	5.15	5.05	5.98	5.51
	Al	1.43	0.65	1.45	1.30	1.08	0.83	0.53	0.85	0.95	0.02	0.49
	Total	6.00	6.00	6.00	6.00	6.00	6.00	6.00	6.00	6.00	6.00	6.00
<i>V</i>	O	3.00	3.00	3.00	3.00	3.00	3.00	3.00	3.00	2.90	2.59	3.00
	OH	-	-	-	-	-	-	-	-	0.10	0.41	-
	Total	3.00	3.00	3.00	3.00	3.00	3.00	3.00	3.00	3.00	3.00	3.00
<i>W</i>	O	0.95	0.93	0.72	0.80	0.81	0.76	0.94	0.44	0.98	0.78	0.63
	OH	0.05	0.07	0.28	0.20	0.19	0.24	0.06	0.56	-	-	0.23
	F	-	-	-	-	-	-	-	-	0.02	0.22	0.14
	Total	1.00	1.00	1.00	1.00	1.00	1.00	1.00	1.00	1.00	1.00	1.00

Note: * - numbers are those from Figure 1, bdl – below detection limit. 1AD-23 and 2AD-23 are data for crystals used for SCXRD.

Table 2. Crystal parameters, data collection and structure refinement details for the studied tourmaline and some related species

Crystal data	This work		Nishio-Hamane et al., 2014	Scribner et al., 2021		Bačík et al., 2013
	1AD-23	2AD-23		Italy	Canada	Zlatá Idka
Crystal system, space group	Trigonal, $R3m$					
a (Å)	15.9811(2)	15.9621(3)	15.9290(2)	15.9270(10)	15.9910(3)	15.916(3)
c (Å)	7.12520(10)	7.14110(10)	7.1830(1)	7.1270(5)	7.2224(2)	7.1071(12)
V (Å ³)	1575.94(5)	1575.71(6)	1578.39(4)	1565.7(2)	1599.42(7)	1559.1(4)
Z	3					
Data collection and refinement						
Diffraction	Rigaku		Bruker	Bruker		Oxford Diffraction
	XtaLAB Synergy-S		SMART CCD	X8 APEX II		KM-4 Xcalibur
Radiation	Mo $K\alpha$					
No. of measured, independent and observed [$I > 2\sigma(I)$] reflections	10149, 1588, 1557	11511, 1392, 1385	5589, 1886	9398, 1273, 1225	21660, 3214, 2953	3174, 1474, 1111
R_{int} , R_σ	0.029, 0.016	0.035, 0.017	0.040	0.050, 0.033	0.042, 0.033	
$2\theta_{max}$ (°)	71	68	80	63	91	72
R_1 , wR_2 , S	0.017, 0.047, 1.101	0.017, 0.045, 1.119	0.038, 0.093, 1.09	0.019, 0.042, 1.07	0.031, 0.056, 1.052	0.034, 0.066, 0.84
$\Delta\rho_{max}$, $\Delta\rho_{min}$ (e Å ⁻³)	0.57, -0.35	0.46, -0.35	1.19, -0.80	0.31, -0.44	1.10, -1.10	0.67, -0.38

Table 3. Bond lengths (Å) in main polyhedrons and polyhedral volumes (Å³) of the studied tourmaline in comparison with published data

	This study		Nishio-Hamane et al., 2014	Scribner et al., 2021		Bačík et al., 2013
	1AD-23	2AD-23		Italy	Canada	Zlatá Idka
<i>X</i> - O2 [3x]	2.542(2)	2.525(2)	2.556	2.526(3)	2.4799(19)	2.561(4)
- O4 [3x]	2.639(2)	2.642(2)	2.736	2.718(3)	2.7774(18)	2.710(3)
- O5 [3x]	2.718 (2)	2.730(2)	2.667	2.635(3)	2.6971(18)	2.781(3)
<i>Mean</i>	2.633	2.632	2.653	2.626	2.652	2.684
<i>Y</i> - O1(<i>W</i>) [1x]	1.949(2)	1.941(2)	1.989	1.930(2)	2.0112(19)	1.944(3)
- O2 [2x]	2.038(1)	2.036(2)	2.028	2.0255(19)	2.0455(12)	1.981(2)
- O3 <i>V</i> [1x]	2.188(2)	2.175(2)	2.204	2.156(3)	2.175(2)	2.132(3)
- O6 [2x]	1.967(1)	1.969(2)	2.003	1.9554(19)	2.0270(12)	1.965(2)
<i>Mean</i>	2.025	2.021	2.043	2.008	2.055	1.995
<i>Z</i> - O3(<i>V</i>) [1x]	1.996(1)	1.995(1)	1.978	1.8838(18)	1.9871(9)	1.9890(15)
- O6 [1x]	1.870(1)	1.878(2)	1.867	1.9007(18)	1.8953(12)	1.869(2)
- O7 [1x]	1.876(1)	1.885(1)	1.941	1.8858(18)	1.9728(12)	1.876(2)
- O7 [1x]	1.926(1)	1.936(1)	1.883	1.9223(19)	1.9728(12)	1.925(2)
- O8 [1x]	1.903(1)	1.903(1)	1.895	1.9325(18)	1.9027(12)	1.889(2)
- O8 [1x]	1.927(1)	1.925(1)	1.930	1.9943(13)	1.9346(13)	1.918(2)
<i>Mean</i>	1.916	1.920	1.916	1.920	1.933	1.911
<i>T</i> - O4 [1x]	1.665(1)	1.662(1)	1.633	1.625(2)	1.6328(7)	1.6412(15)
- O5 [1x]	1.646(1)	1.642(1)	1.653	1.6160(18)	1.6496(8)	1.6298(12)
- O6 [1x]	1.639(1)	1.630(2)	1.630	1.6389(11)	1.6019(12)	1.633(2)
- O7 [1x]	1.630(1)	1.621(1)	1.619	1.6584(13)	1.6034(11)	1.625(2)
<i>Mean</i>	1.645	1.639	1.634	1.634	1.622	1.632
<i>B</i> - O2 [1x]	1.391(3)	1.387(3)	1.378	1.372(3)	1.380(3)	1.380(6)
- O8 [2x]	1.373(2)	1.374(2)	1.369	1.383(5)	1.3754(16)	1.373(3)
<i>Mean</i>	1.379	1.378	1.372	1.376	1.377	1.375

Note: the numbers in square brackets correspond to frequency of bonds.



Figure 1. The studied tourmaline: (a) crystals (black) in bedrock (with label), (b) equant crystals, (c) dissolved Si-rich zones (dark) inside Si-poor crystal (BSE-image), (d) Si-rich zone inside Si-poor crystal (BSE-image). Number are as in Table 1 and Figure 2

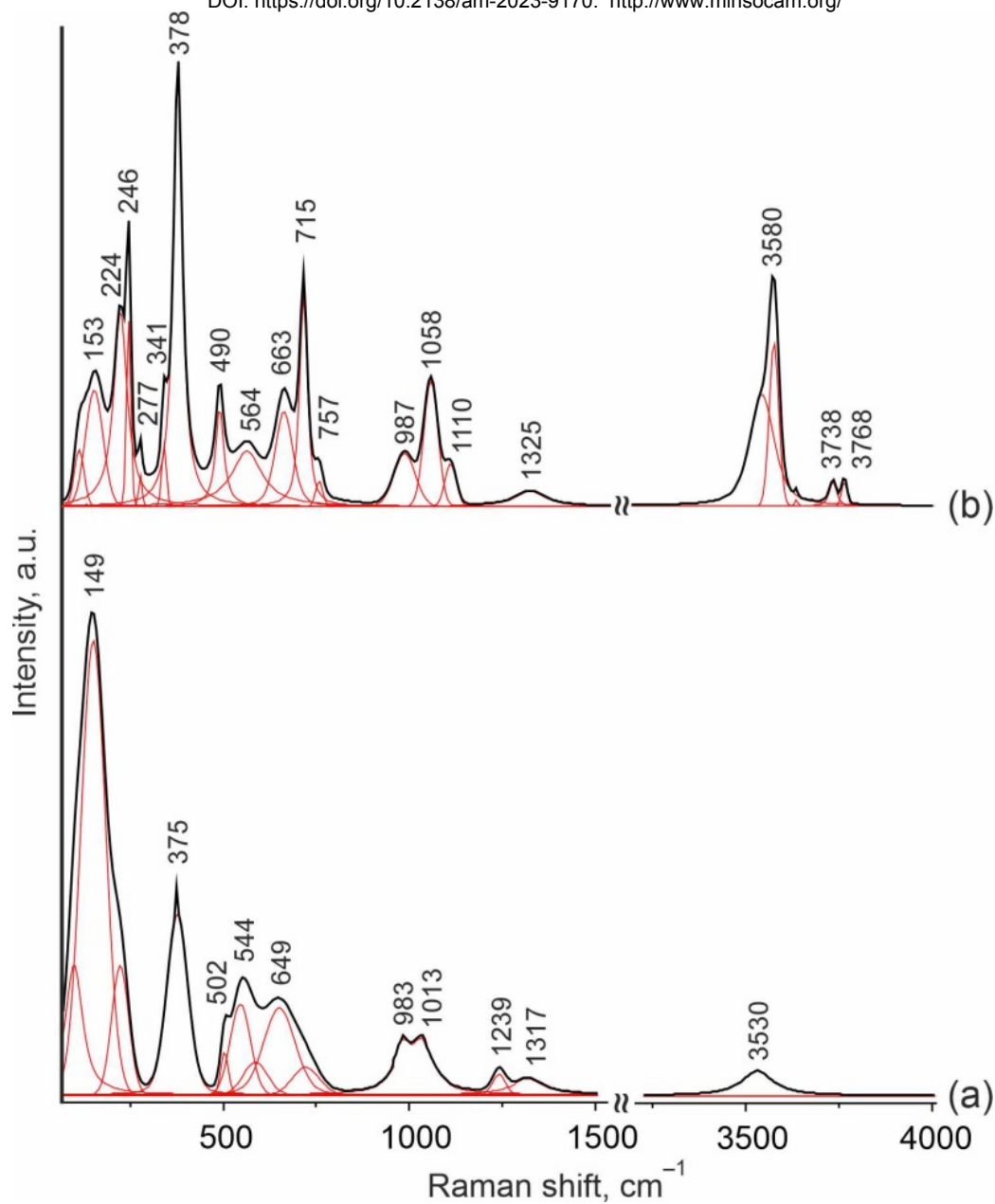


Figure 2. The Raman spectra of the studied tourmaline: (a) – Si-poor zone (No 1; Figure 1), (b) – Si-rich zone (No 2; Figure 1). The black line shows the experimental data, red line — peak deconvolution.

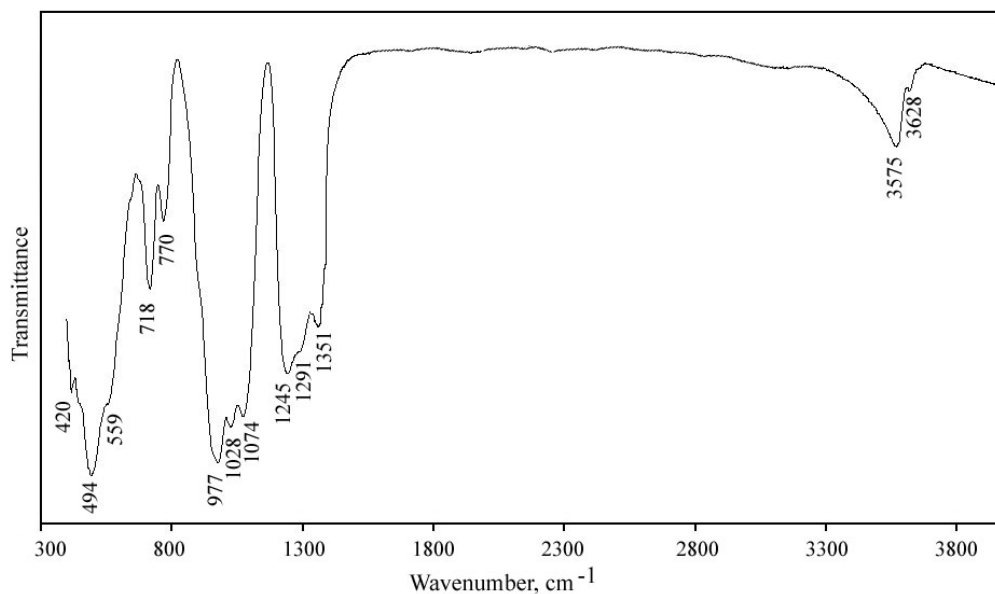


Figure 3. Powder infrared absorption spectrum of the studied tourmaline.

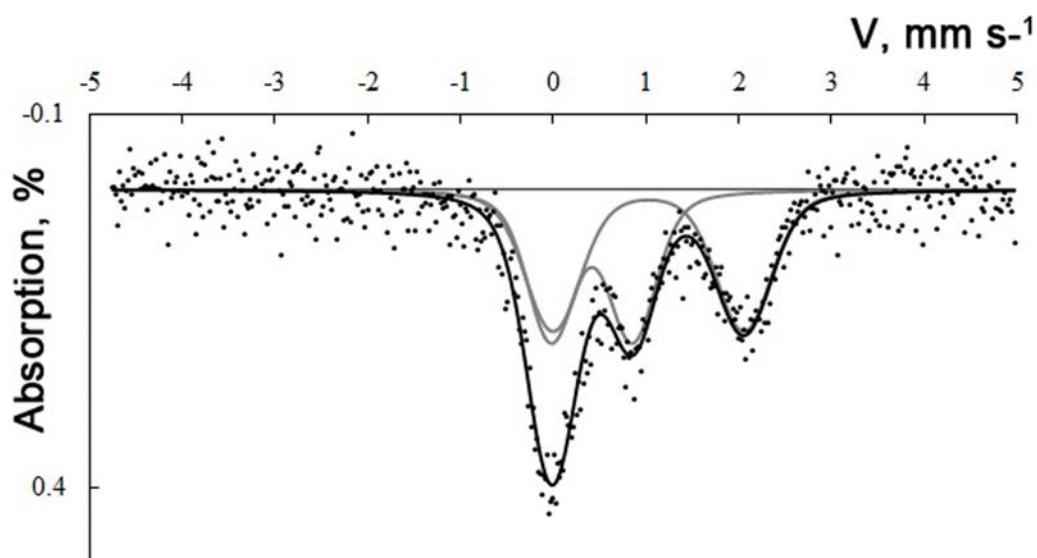


Figure 4. Room-temperature Mössbauer spectrum of the studied tourmaline.

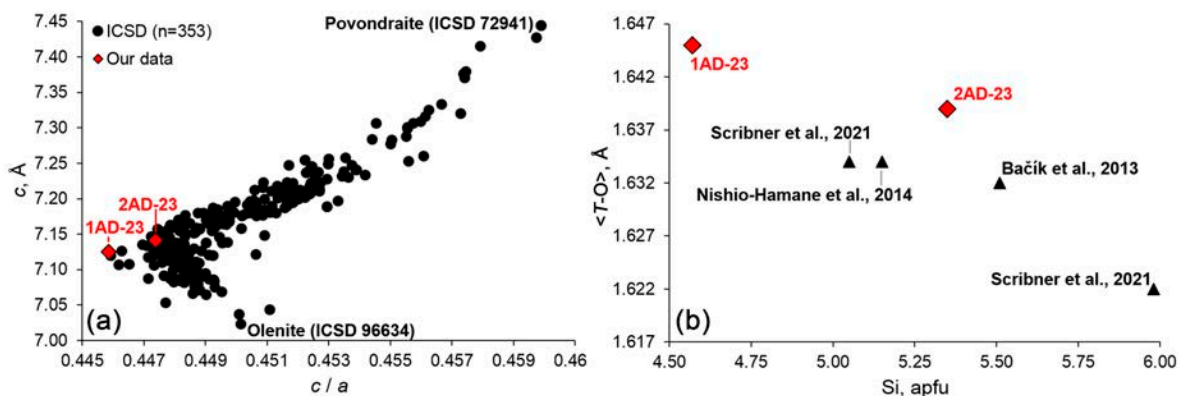


Figure 5. Crystallographic data on the studied tourmaline in comparison with published data: (a) – c unit cell parameter vs. c/a ratio, (b) – $\langle T-O \rangle$ distance vs. Si apfu. Note ICSD - Inorganic Crystal Structure Database (accessed 05.08.2023)

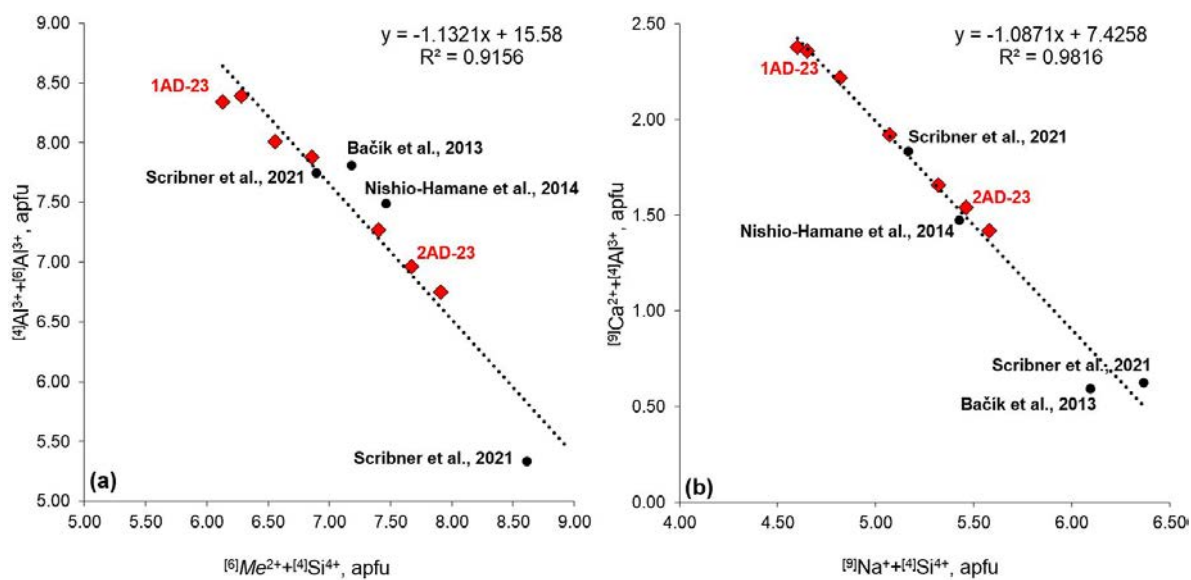


Figure 6. Chemical composition data on the studied tourmaline in comparison with published data: (a) – $[6]Al^{3+} + [4]Al^{3+}$ vs. $[6]Me^{2+} + [4]Si^{4+}$, (b) – $[9]Ca^{2+} + [4]Al^{3+}$ vs. $[9]Na^{+} + [4]Si^{4+}$. Note: black circles correspond to literature data, red diamonds correspond to our data.